Representative Volume Elements for Plasticity and Creep Measured from High-Resolution Microscale Strain Fields

R.B. Vieira[1], H. Sehitoglu[2], J. Lambros[1,2,*]

[1]Aerospace Engineering, University of Illinois at Urbana-Champaign, Urbana, 61801, IL.
[2]Mechanical Science and Engineering, University of Illinois at Urbana-Champaign, Urbana, 61801, IL.
* corresponding author: lambros@illinois.edu

Abstract

Homogenization techniques have been widely used in upscaling microscale numerical results to predict the macroscopic response of materials. Often homogenization is based on the concept of a representative volume element (RVE) and thus, measuring the RVE size and understanding what factors influence it are key elements in successful material modeling. Here, the size of the RVE for an austenitic stainless steel alloy is experimentally determined under, both separately and combined, plasticity and creep loading conditions with varying parameters (namely stress, temperature, and creep hold time). We use a high-resolution optical digital image correlation (DIC) methodology capable of discerning residual strain inhomogeneities at the microstructural level. Furthermore, by combining the strain results from DIC with surface microstructural information from electron backscatter diffraction (EBSD), the localized strains near grain boundaries can be isolated allowing for quantitative observations related to the deformation mechanisms responsible for strain accumulation. Finally, by comparing the results for RVE size and localized normal to shear strain ratios for different combinations of loading parameters, the relationship between grain-boundary sliding and the resulting heterogeneity of the strain field is explored. Cases where grain-boundary sliding was the dominant deformation mechanism (i.e., at elevated temperature) had considerably smaller RVE sizes (from 4 to 6 times the average grain size) when compared to samples where sliding was not as prevalent (around 10 times the average grain size).

Keywords: Representative volume element, creep, plasticity, deformation inhomogeneities

Acta Materialia

1. Introduction

Through both experimental and numerical efforts, highly inhomogeneous deformation has been widely observed to occur at the microscale of polycrystalline metals. Such heterogeneity can ultimately be attributed to the underlying mechanisms of deformation that govern the interactions between anisotropic grains. Experimental studies regarding micro and mesoscale strain inhomogeneities in titanium [1], copper [2] and aluminum [3] have shown the development of plastic heterogeneity at the grain level. Many such experimental studies have been used to validate corresponding numerical models such as crystal plasticity simulations. However, in order to reduce computational requirements and to connect to the macroscale, such simulations often take advantage of homogenization techniques that allow the use of local constitutive response of the material to extrapolate the macroscopic response [4]. A central concept of many such techniques is the representative volume element (RVE), described by Hill [5] as being "entirely typical of the whole mixture on average" and containing "a sufficient number of inclusions for the apparent overall moduli to be effectively independent of the surface values of traction and displacement, so long as these values are macroscopically uniform.".

An extensive series of studies regarding the determination of RVE length scales have been published in the literature, with a wide range of results. A majority of these studies were conducted through numerical approaches that usually determine the RVE size through homogenization techniques, where the result obtained from a simulation has to converge to the macroscopic result for a large enough simulation box [6-9]. Experimental studies, such as the one conducted by Efstathiou et al. [1], are far fewer. Efstathiou et al. [1] experimentally determined the RVE size of a plastically loaded titanium alloy to be ~30 times the average grain size. Ravindran et al. [10] present an overview of RVE sizes obtained for different polycrystalline materials. They also proposed their own method of experimentally measuring RVE sizes, finding that, for a plastically loaded carbon steel, the RVE size was 8.85 times the average grain size. More recently, Stinville et al. [11, 12] experimentally measured RVE sizes of a nickel superalloy for plastic strain localization (~9 times the average grain size) and fatigue crack initiation (~34 times the average grain size), pointing to the possibility that the size of the RVE depends on the investigated property, as well as on the loading parameters. The possibility of property-dependent RVE sizes has also been investigated in recent studies by Bagri et al. [13], where they found differences in the microstructure-based RVE size and property-based RVE size, pointing that different properties could result in different RVE sizes. Yang et al. [14], predicted RVE sizes for viscoplastic properties of FCC Cu to be consistently larger than those for elastic properties, thus concluding that loading parameters such as stress play a role in the RVE size. Therefore, RVE sizes can be property-dependent as well as load-dependent.

The concept of the RVE has also been used in studies with the goal of uncovering the underlying mechanisms of deformation. Githens et al. [15] used crystal plasticity simulations to help interpret the various slip traces observed in the dense Digital Image Correlation (DIC) data as variations in slip and twin activity within each grain of a magnesium alloy. Motaman et al. [16] investigated the connections between process-induced microstructural properties and the macroscopic response of an additively manufactured metal, through the combination of experimental observations of the grain structure and a full-field method for computational polycrystal homogenization combined with physics-based crystal plasticity modelling. Raabe et al. [3] also investigated the effects of grain-scale plastic heterogeneity on experimental and simulation data of the macro and micromechanical response of a polycrystalline aluminum sample.

In the present work, the relationship between the heterogeneous micromechanical strain accumulation of a polycrystalline austenitic stainless steel and the creep and plasticity loading conditions to which it is subjected, known to control underlying deformation mechanisms, is investigated. Pelleg [17] presents a comprehensive review of such mechanisms responsible for creep and general inelastic deformation. To this end, experimentally determined RVE sizes are used as a quantitative mesoscale measure of the degree of inhomogeneity and are posteriorly compared with observations on the localized grain-boundary response for varying loading condition (maximum stress, temperature and hold times), which can be related to the underlying deformation mechanisms, such as grain-boundary sliding (a well-documented creep mechanism, as discussed by Bell and Langdon [18]). The RVE sizes are measured through the use of a high-resolution optical DIC technique that allows for measurements of residual strains at the grain scale. The specific goals of the analysis are to:

1) Study the relationship between RVE sizes and loading conditions namely, plasticity and creep, both individually and combined;
2) Observe if and how RVE sizes are affected by changes in loading temperature;
3) Explore possible relationships between RVE sizes and the underlying deformation mechanisms.

2. Experimental Methods

2.1 Material and Sample Preparation

Austenitic stainless steel 709, an alloy being considered as a candidate for applications in sodium fast reactors [19], is the material investigated throughout this work. The macroscopic behavior of alloy 709 is similar to the well-known 316 stainless steel, but it presents improved properties in some high-temperature applications. Both macro and microscopic investigations of tensile [20-22], fatigue, and creep [23, 24] properties of alloy 709 are available in the literature. For the proposed experimental investigations of the relationships between the microscale strain accumulation (at the grain scale) and the mesoscale response of the material (as measured by the RVE size), dog-bone samples (Fig. 1 (a)) were machined from the as-received material and loaded under plasticity and creep conditions in various combinations and at different temperatures. Fig. 1 also shows an example of the DIC speckle pattern for both in in situ images ((b) and (d)) and ex situ high-magnification images ((c) and (e)), before and after deformation, respectively, described in detail in the next section.

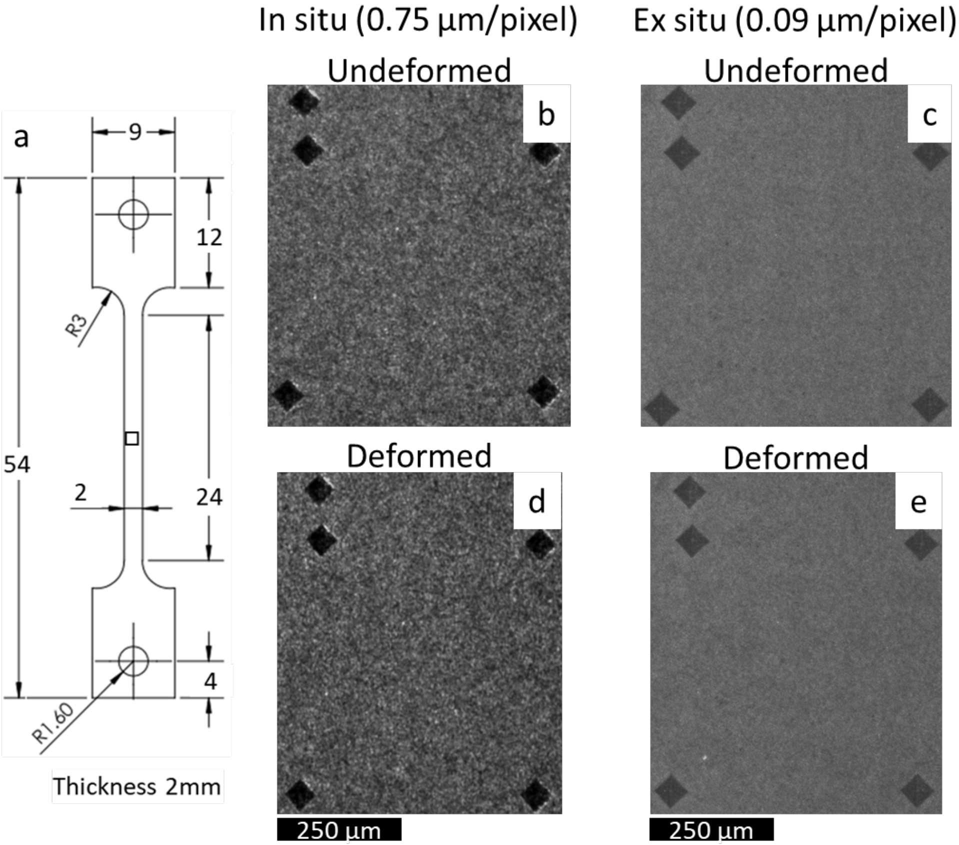

Fig. 1. (a) Dog-bone sample dimensions in *mm*; (b, d) DIC speckle pattern before and after deformation as seen from in situ imaging (0.75 µm/pixel); (c, e) DIC speckle pattern before and after deformation as seen from ex situ imaging (0.09 µm/pixel).

2.2 Grain-scale Strain Measurement

The grain-scale strain measurements presented in this work were obtained using an adapted version of the technique developed by Carroll et al. [25]. The widely used technique of digital image correlation (DIC) can be applied to obtain full-field displacement (and strain) measurements on a surface. The correlation of undeformed and deformed images of a surface covered by a random speckle pattern allows for displacement field measurements with no inherent limitations on spatial resolution [26]. Taking advantage of such capability, DIC can be used across multiple length scales, as long as images of sufficient resolution can be obtained. The main difference from the technique described in [25] was the introduction of an intermediate step in the procedure used to align the microstructure obtained from electron backscatter diffraction (EBSD) scans with the strain data obtained from DIC, as described below. The speckle pattern application followed a similar procedure, by depositing 10μm SiC particles on the surface using compressed air, to obtain the speckle patterns shown in Fig. 1(b-e).

With the aim of studying the grain-scale behavior of alloy 709 with an average grain size between 25 and 30 μm, high-resolution images of the surface were taken under an optical microscope. An objective lens with 40x magnification (Olympus SLCPlanFl 40x) was used for all the experimental results shown in the next sections, resulting in ~0.09 μm/pixel resolution images. The obvious downside of this approach is the reduced field of view size (190x190 μm FOV using a 2000x2000 pixel camera). To account for this, grids of 6 by 6 images (with a 50% overlap) were taken covering the entire region of interest. Before correlation, these images were stitched together using the built-in algorithm in Fiji ImageJ [27], with the significant overlap between the images helping to minimize any stitching distortions. All results shown here were obtained from correlations with subset size of 61 pixels (~5.5 μm) and a step size of 10 pixels (~0.9 μm), allowing for an average of about 5 subsets along the width of an average grain (25-30 μm). The average grain size was obtained from electron backscatter diffraction (EBSD) results, using the built-in line intercept algorithm from the MTEX open source toolbox. The selection of DIC parameters was done by selecting the smallest subset size for which correlation was successful in the entire region of interest (i.e., without gaps in the resulting displacement fields), while the correlation point step size was fixed at 10 pixels. Although an in-depth sensitivity analysis such as the one presented by Rajan et al. [28] will in general improve correlation results, it is probably less useful in our case because of the high average strain levels reached in all of tested cases (plastic deformation was present in all experiments), for which the relative errors from DIC are not as significant. However for probing smaller strain levels than those in this work, the results could be improved using the methodology presented in [28].

The correlation between the undeformed (reference) and deformed images was done using the commercially available DIC software Vic2D (from Correlated Solutions). The strain fields were obtained by differentiating the displacement fields resulting from the correlation using a central difference approach, as described by

$$\begin{cases} \varepsilon_{xx}(x,y) = \frac{U(x+step)-U(x-step)}{2\cdot step} \\ \varepsilon_{yy}(x,y) = \frac{V(y+step)-V(y-step)}{2\cdot step} \\ \varepsilon_{xy}(x,y) = \frac{1}{2}\cdot\left(\frac{U(y+step)-U(y-step)}{2\cdot step} + \frac{V(x+step)-V(x-step)}{2\cdot step}\right) \end{cases}, \tag{1}$$

where *U* and *V* are the horizontal and vertical displacement components along *x* and *y*, the horizontal and vertical coordinates, and *step* is the step size (10 pixels). A central difference scheme was used so as to minimize the smoothing performed during differentiation so that highly detailed strain fields capable of better capturing local strain gradients could be obtained–though possibly also containing noiser data. However, the strain noise floor associated with the selected

DIC parameters was measured to be below 10^{-4}, resulting in an acceptable signal-to-noise ratio for all the studied plasticity and creep experiments. In the event that the measured strain signal is comparable to the noise floor, such as for example in the work of Koohbor et al. [29] where the signal-to-noise ratio of strains measured during tensile testing of woven composites was of the order of magnitude of the applied strains, additional strain smoothing techniques may be necessary to reduce the noise levels.

In order to investigate the influence of microstructural parameters on strain-accumulation, EBSD scans of the surface were taken prior to testing. EBSD is a widely used technique that produces crystal orientation maps of a sample's surface [30]. The EBSD scans shown throughout this work were obtained with a distance between measurement points of 1 μm, using a JEOL 7000F SEM. The surface of the samples was prepared for EBSD through polishing using silicon carbide paper down to 1200 grit, followed by diamond suspensions down to 0.5 μm and a final step inside a vibratory polisher with a commercial colloidal silica solution for 3 hours.

Combining these two datasets (from DIC and EBSD) requires an alignment procedure that was performed through the use of fiducial Vickers markers placed at the edges of the region of interest. Although the markers were visible in both the DIC and EBSD images, some distortions are present in the EBSD scan results. To account for these distortions a set of alignment optical images were taken at the same magnification as the DIC images *before* applying the DIC pattern, but *after* etching with a 36% weight of solute / weight of solution of HCl in water, for 15 minutes at 100 °C. This intermediate alignment step uses the strength of each technique to enhance the final positioning of the strains within the microstructure, with optical microscopy being more precise in the positioning of the grains within the DIC reference frame and EBSD being more reliable in capturing all the existing grain boundaries.

Fig. 2 shows a representative set of images used to align the microscale strains to the microstructure. Fig. 2(a) shows an EBSD map, colored by the first Euler angle. Fig. 2(b) shows the grain boundaries extracted from the EBSD results by considering differences in average crystal orientation >7°. Fig. 2(c) shows the optical image (stitched grid of images) taken of the etched surface. The alignment between Fig. 2(b) and (c) is done by selecting prominent grain-boundary features visible in both images (e.g., triple points) and fitting a projective transformation to these points. For this type of transformation, all straight lines remain straight, but parallelism is not conserved. Fig. 2(d) shows the reference image (stitched grid of images) for DIC, which establishes the coordinate system where the results of the correlation are computed. Finally, the alignment between Fig. 2(c) and (d) is done by selecting the corners of the fiducial markers seen on both images and fitting an affine transformation (for which both straightness and parallelism are conserved) to those points. These two transformations can then be used consecutively to align the EBSD results into the DIC reference frame. The average error on the positioning of the grain boundaries was estimated to be at most half the thickness of the etched grain boundaries, i.e., at around 5 pixels or 0.45 μm, which is considerably smaller than both the average grain size (25-30 μm) and the DIC spatial resolution (subset sizes around 5.5 μm). In the alignment process used in [24] no image comparable to Fig. 2(c) was taken and a comparison was made directly between Fig.2 (b) and Fig. 2(d). The new step of the introduction of the optical data in Fig. 2(c) was done here to improve the accuracy of aligning the DIC and EBSD datasets since we are interested in identifying strain features very near grain boundaries.

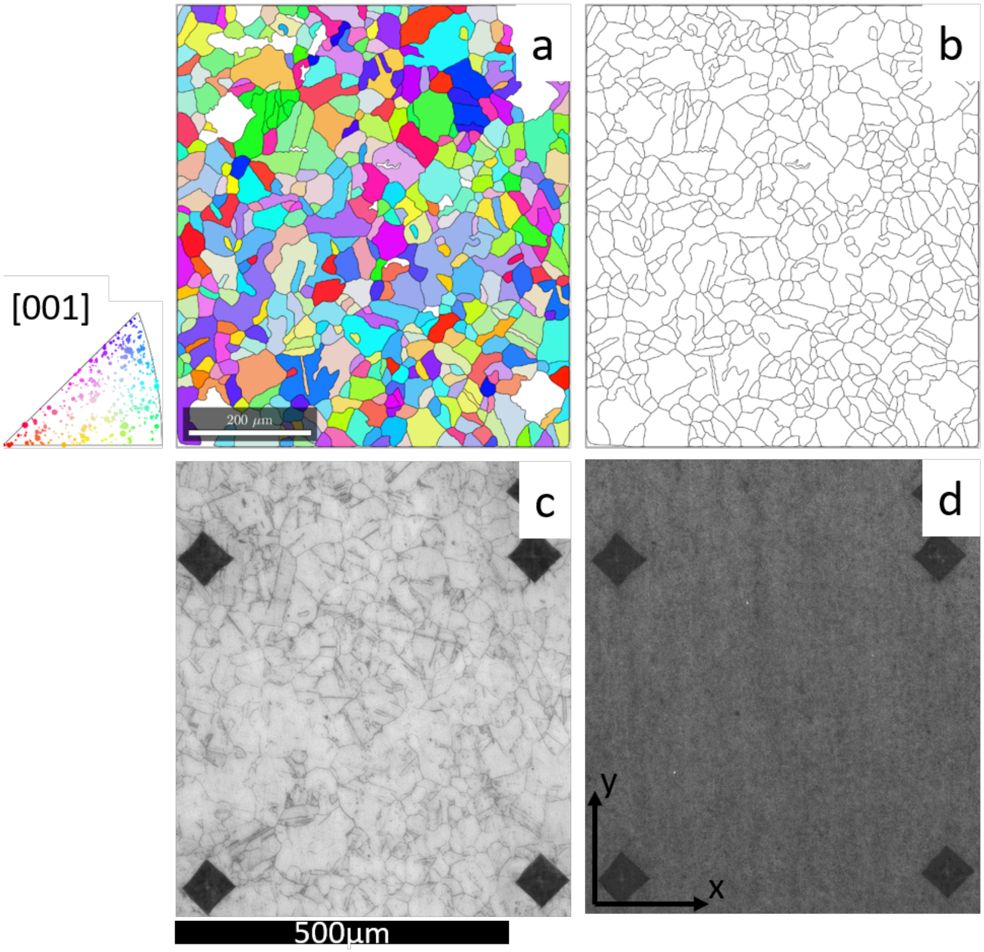

Fig. 2. (a) Resulting map from EBSD, colored by the first Euler angle (b) Grain boundaries obtained from the EBSD results; (c) Optical image of the etched surface; and (d) DIC reference image with the reference frame drawn.

2.3 Creep and plasticity loading

All experiments discussed in the following sections were conducted using an Instron servo-hydraulic machine. The photograph in Fig. 3 shows the equipment used for high-temperature creep and plasticity experiments. An infrared thermometer (A) was used to measure the temperature of the region of interest of the sample without contacting the surface; an induction heater (B), along with the input temperature from the thermometer, was used to heat the sample and control the temperature during experimentation; a CCD camera (C) was used to image the sample's surface in real time and the resulting images along with DIC were used to measure macroscale in situ strains during the stress controlled experiments; a set of cooled grips (D) (with specifically designed loading fixtures) and an induction heater coil (E), as shown in the accompanying schematic, was used to keep the temperature inside the region of interest within a ±1 °C range.

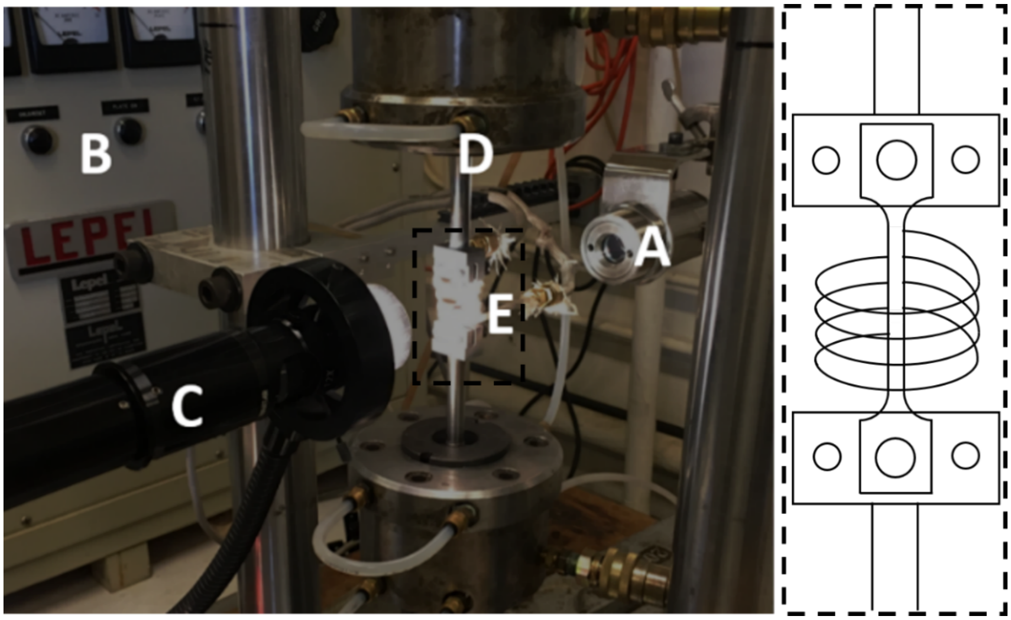

Fig. 3. Loading frame setting. A – Infrared thermometer; B – Induction heater; C – In situ DIC camera and lens; D – Cooled grips; E – Induction heater coil around sample (as shown in schematic).

Samples were tested under different loading histories in order to explore the behavior of alloy 709 under the following three proposed types of deformation: ***plasticity*** when the sample was subjected to a stress above macroscopic yield at the test temperature, without being subjected to any amount of hold time before unloading; ***elastic creep*** for a loading step in which the sample was loaded below yield at the test temperature, being subjected to some extent of hold time at maximum stress; and the combination of plasticity and creep, where a sample was loaded above yield at the test temperature and subsequently subjected to some hold time at maximum stress in what we will refer to henceforth as ***plastic creep***. Fig. 4 shows schematic stress vs. strain curves displaying the characteristics of the three different types of deformation investigated.

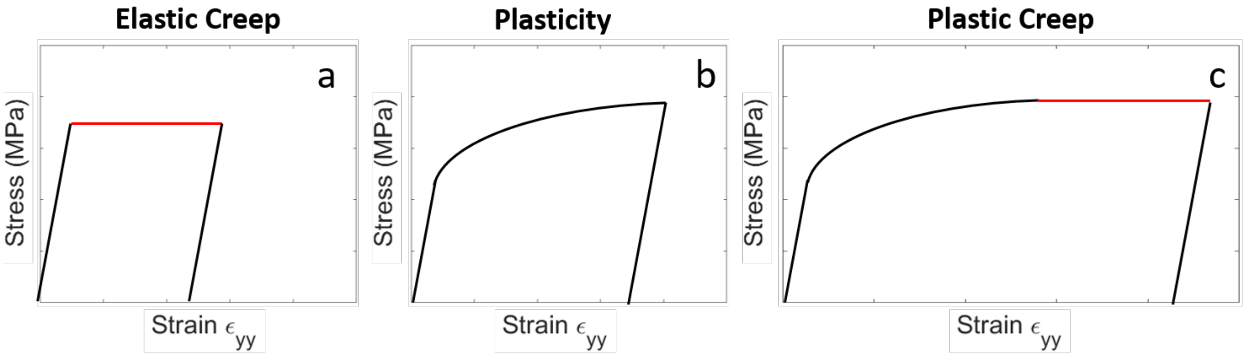

Fig. 4. Schematic stress-strain curves of the three types of deformation investigated; (a) Elastic creep; (b) Plasticity and (c) Plastic creep.

The particular loading parameters involving these three types of deformation for a number of specific cases investigated are listed in Table 1. By varying the maximum stress and the temperature during loading, each sample was subjected to a different deformation type, as listed in the table. The maximum stresses were taken at 25% above or below the macroscopic yield stress for a given temperature depending on whether plastic deformation was desired or not. The yield stress at room temperature was 315 MPa, while at 300°C it was 285 MPa, 200 MPa at 500°C and 110 MPa at 800°C.

Table 1. Loading parameters used for each sample.

Sample	Temperature (°C)	Max Stress (MPa)	Hold Time (min)	Deformation type
1	23	400 (~25% above yield)	0	Plasticity
2	23	400 (~25% above yield)	60	Plastic Creep
3	300	215 (~25% below yield)	60	Elastic Creep
4	300	350 (~25% above yield)	0	Plasticity
5	300	350 (~25% above yield)	60	Plastic Creep
6	500	150 (~25% below yield)	60	Elastic Creep
7	500	250 (~25% above yield)	0	Plasticity
8	500	250 (~25% above yield)	60	Plastic Creep
9	800	80 (~25% below yield)	60	Elastic Creep

3. DIC Results and Representative Volume Element Measurements

3.1 Residual strain fields

After loading, each sample enumerated in Table 1 was removed from the loading frame and placed under the microscope to have a set of deformed images taken. The result from the subsequent DIC correlation is a set of residual surface strain fields, as for example shown in Fig. 5(b) for sample 1. Fig. 5(a) shows a schematic of the stress-strain curve of the loading to which sample 1 was subjected, at room temperature, with a maximum stress ~25% above yield (400 MPa) and with no hold time leading to plastic deformation. Fig. 5(b) shows the residual axial strain (ε_{yy}) field after loading.

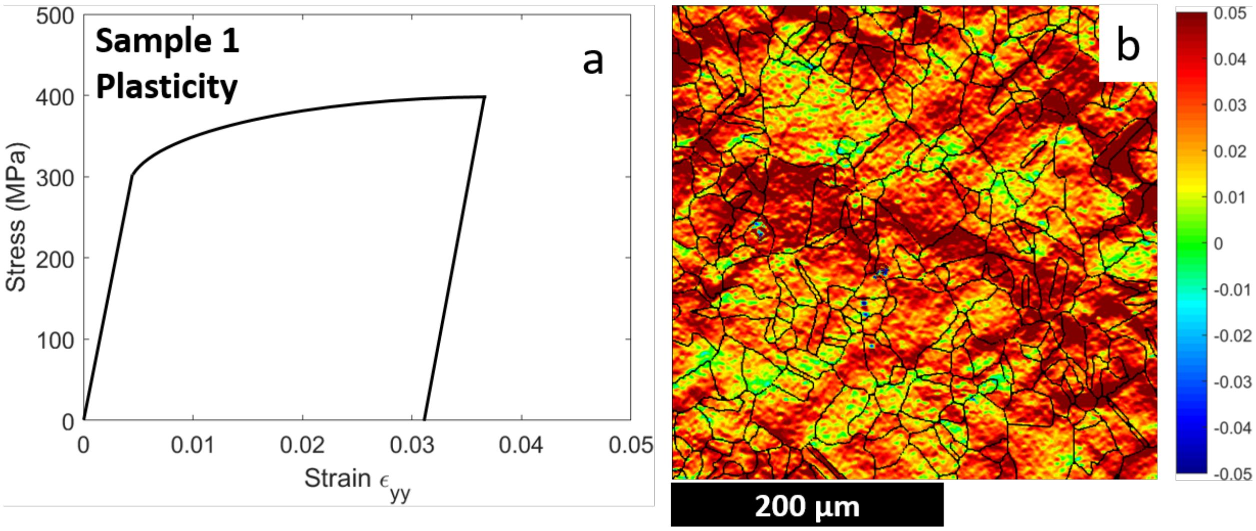

Fig. 5. (a) Schematic stress strain curve for sample 1; (b) Residual axial strain field (ε_{yy}) obtained after loading.

From Fig. 5(b) we see that at this length scale, strains accumulate at preferential locations, resulting in a highly inhomogeneous residual strain field. Furthermore, the residual strain levels at specific points reach values much higher than the macroscopic strain, with the maximum local strain measured being at around 8% (0.08), while the macroscopic strain is just above 3% (0.0309). Also, as has been observed before [31], grain boundaries appear to present "hot-spots" for strain accumulation. Finally, the appearance of deformation bands at a 45° angle from the loading direction was observed, similar to what has been reported by previous authors for plastically deformed austenitic stainless steels [32, 33]. Fig. 6 shows the equivalent results for sample 3, which was subjected to loading at 300°C, with a maximum stress ~25% below yield (215MPa) held for 60 minutes, i.e. it underwent elastic creep.

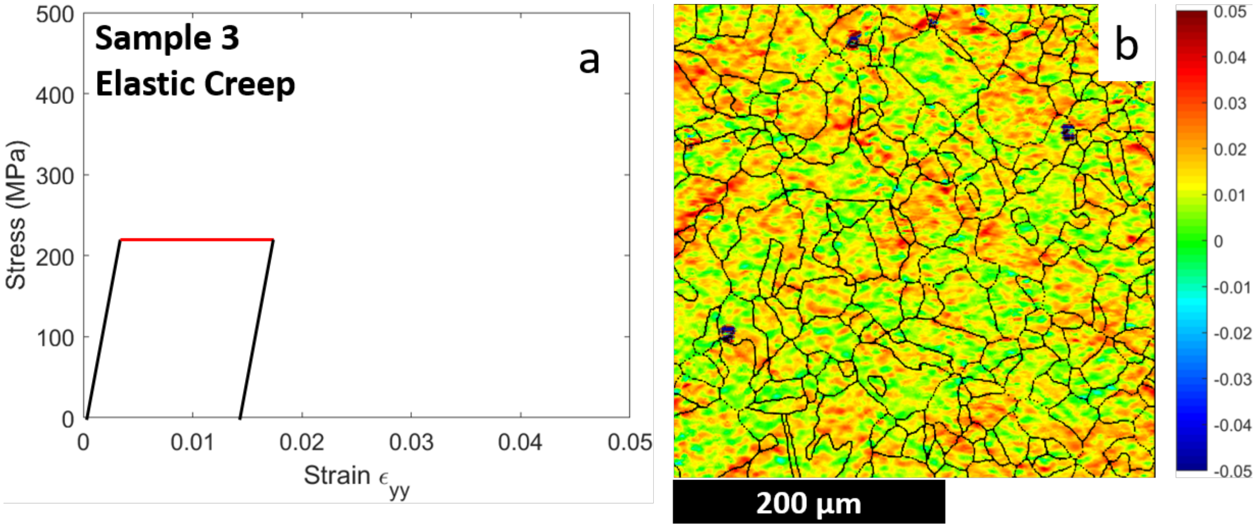

Fig. 6. (a) Schematic stress strain curve for sample 3; (b) Residual axial strain field (ε_{yy}) obtained after loading.

From these results it is clear that the strains accumulated during 1 hour of elastic creep at 300°C (maximum stress 25% below yield) were much lower than the strains accumulated after plastic loading at room temperature (25% above yield). Again, the resulting strain field was highly inhomogeneous, although to a lesser extent than before, at least visually. Fig. 7 shows the corresponding results obtained from sample 8, which was loaded at 500°C, with maximum stress ~25% above yield (250MPa) held for 60 minutes, i.e. underwent plastic creep. Again, the resulting residual strain field is highly inhomogeneous, but it is hard to compare the degrees of inhomogeneity of each sample as well as the locations where strains tend to accumulate. The underlying factors that determine the position of these preferential spots for strain accumulation must be related to the microstructural parameters, but also might be related to the deformation mechanisms responsible for straining. Then, the hypothesis explored in the next sections is that the degree of inhomogeneity is controlled by the underlying deformation mechanisms, which in turn are a function of loading parameters, such as temperature and maximum stress.

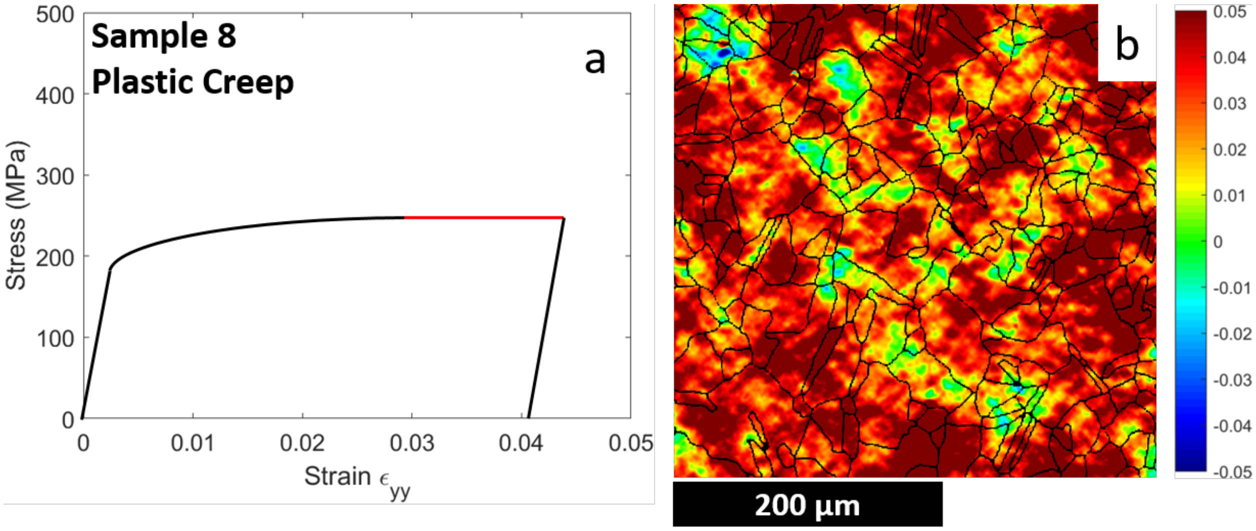

Fig. 7. Schematic stress strain curve for sample 8; (b) Residual axial strain field (ε_{yy}) obtained after loading.

3.2 Representative volume element (RVE) measurement

In order to quantify the inhomogeneity of the strain fields, the concept of the representative volume element is introduced. The RVE can be understood as the smallest material element that is capable of reflecting an average "property" of the given bulk material. The "property" can be a microstructural feature (e.g., grain size); it can be a mechanical property (e.g., yield strength, modulus) or it can be a material response (e.g., strains resulting from stress) [13]. The novel methodology used here to experimentally measure RVE sizes for strain inhomogeneity is detailed in [34]. A brief explanation of this methodology, which emphasizes the statistical nature of an RVE, is given here and is illustrated in Fig. 8. The approach consists of selecting randomly positioned boxes from within the strain field, as illustrated in Fig. 8(a), and plotting histograms of the average strain from all boxes. This procedure is repeated for varying box sizes, all the way from a 1 by 1 pixel box to a box the size of the entire strain field. Fig. 8(b) shows examples of the resulting histograms obtained for boxes of sizes 10 by 10, 164 by 164 and 289 by 289 µm, for

10,000 boxes. There is a clear trend presented by these images: The boxes of side length of 10 µm result in a histogram with a very wide range of average strains, the histogram obtained from the boxes of side length 164 µm have the average strain from 80% of the 10,000 boxes fall within a ±5% margin from the global average strain, while for the boxes of side length 289 µm the average strain from 80% of the 10,000 boxes fall within a ±1% margin from the global average strain. That is, the larger the box size, the more the box averages converge to the global average residual strain value (0.02 as measured from in situ DIC after unloading).

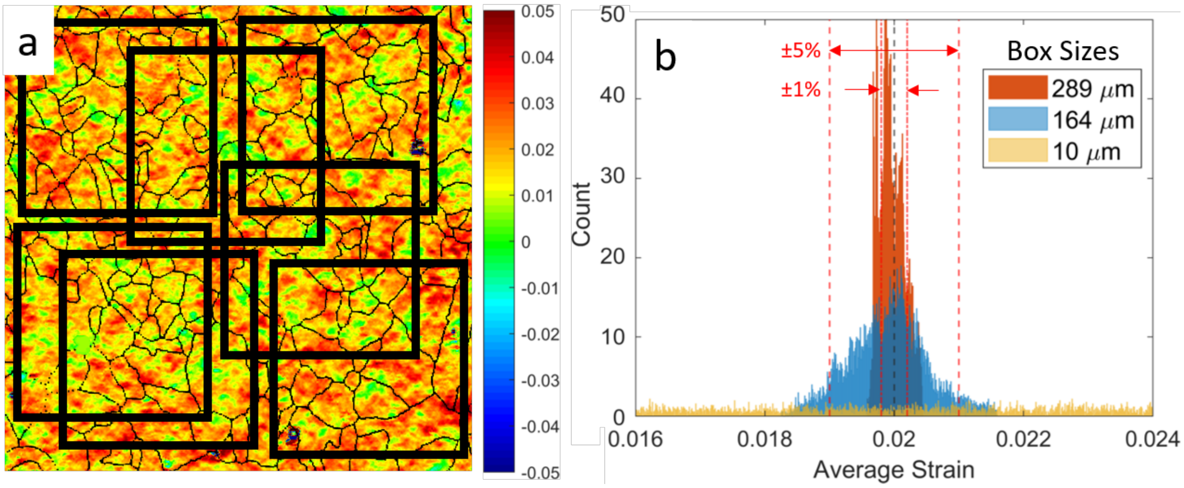

Fig. 8. (a) Residual axial strain field overlaid by a few randomly selected boxes of size 164 by 164 pixels; (b) Histograms for the average strains of 10,000 randomly selected boxes of size 10 by 10, 164 by 164 (80% fall within ±5% margin) and 289 by 289 pixels (80% fall within ±1% margin).

This methodology allows for a statistical measure of the size of an RVE. For all the RVE sizes reported here, the criterion used was that 80% of the boxes had to fall within a ±5% margin from the global average, which is the same as saying that 80% of the time that box size will satisfy the condition of converging to the global average strain (considering a ±5% margin). These margins could be more (or less) restrictive, and the resulting RVE size would be larger (or smaller), thus maintaining the statistical character of the RVE [35]. In the analysis that follows the margins used for all samples are the same, allowing for a relative comparison between the (statistically computed) RVE in each case. Fig. 9 shows a bar plot of the resulting RVE sizes for all of the tested cases, colored by the deformation type. For simplicity, the RVE sizes are reported as a single number, which should be understood as the length of side of the box that satisfies the convergence criteria described earlier. The left vertical axis shows the RVE sizes in μm, while the right vertical axis shows the RVE sizes as a multiple of the average grain size (~27 μm).

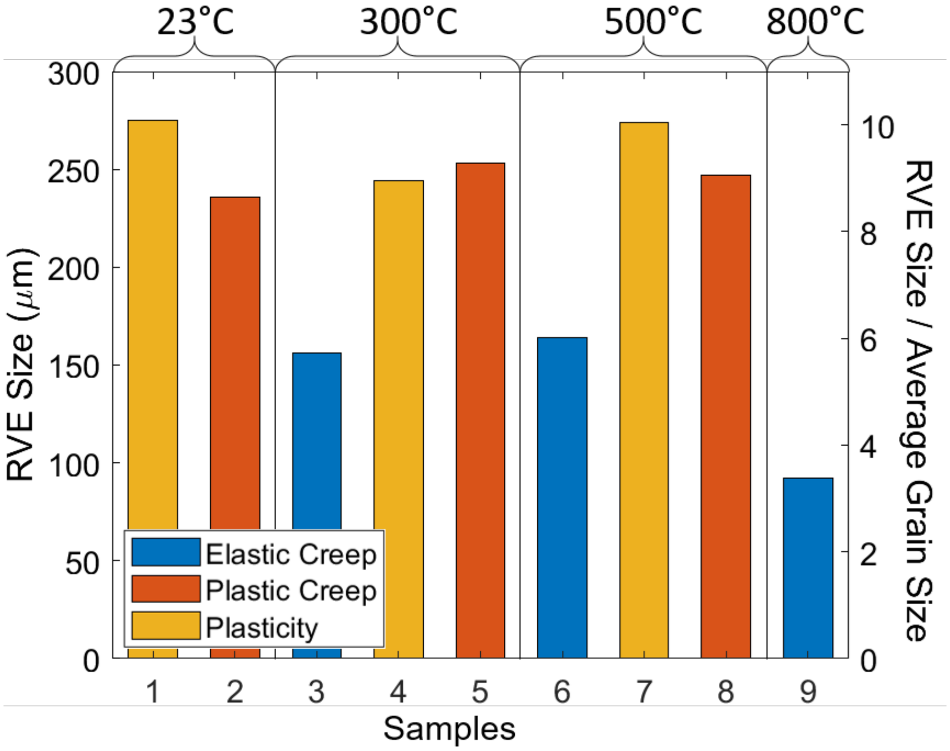

Fig. 9. Bar plot of the resulting RVE sizes for each sample.

All the measured RVE sizes fall within a range from ~4 to ~10 times the average grain diameter along its side. It is clear that the obtained RVE size for *elastic creep* is considerably smaller than that of *plasticity* and *plastic creep*. With the exception of the result obtained for 800°C, the results agree with the literature with regards to the size of measured RVEs (6 to 15 times the average grain size) [11, 36]. Similar differences between plastic and elastic response RVEs as those observed here have also been reported [14]. It is likely that this difference can be attributed to the underlying mechanisms of strain accumulation. Evidence pointing to the relation of RVE with underlying mechanisms can be seen in the difference observed in the development of deformation bands at a 45° angle from the loading direction, with sample 1 having more prominent bands than sample 3, for example. The formation of such strain bands is intrinsically connected to the underlying deformation mechanisms and will necessarily have an effect on the RVE size. Finally, the fact that RVE sizes for *plasticity* and *plastic creep* are very similar leads to the conclusion that plasticity dominates the material behavior (at least under these loading conditions) introducing a higher level of inhomogeneities that overshadows the creep response.

In order to investigate a potential shift in RVE size affected by loading conditions, driven by underlying deformation mechanisms changes, the next section recognizes grain boundaries as the primary locations of higher strain concentration (leading to inhomogeneity) and concentrates at the local strains at regions near grain boundaries, specifically aiming to investigate the relative amounts of normal to shear strains near the boundary regions.

4. Localized Strain Accumulation at Grain Boundaries

When studying strain accumulation at the microscale, the concept of dividing a grain into two regions, mantle (the part of the grain near the boundaries) and core (the grain interior) is useful. The separation of grains into these two sections is motivated by the assumption that the mechanical response of points far enough from grain boundaries shouldn't be influenced by local effects at the boundaries, while points closer to a boundary should have a response governed mainly by their interaction with the boundary [31, 37]. Following this reasoning, to better identify strain accumulation in the mantle regions, strain components in a local coordinate system of the neighboring grain boundaries may be more useful than the axial strains (ε_{yy}) in the global coordinates. Consequently a coordinate transformation from global (sample) coordinates (x, y) to local (grain-boundary) coordinates (normal, n, and tangential, t) is performed based on the EBSD-obtained boundary positions. With this frame rotation it is possible to directly infer what happens at a boundary during loading, specifically the local normal and shear strains can be understood as neighboring grains being pushed together or attempting to slide against each other. The mantle size (region within which the coordinates are transformed) was estimated at 6-7 µm, or around 20% of the average grain size, following the approach of Abuzaid et al. in [31].

The strain coordinate transformation methodology is illustrated in Fig. 10. From the EBSD data set of grain boundaries shown in Fig. 10(a) we selected the closest boundary point (Closest pt. in Fig. 10(b)) to the mantle point of interest (Interrogated pt. in Fig. 10(b)). Subsequently, a set of up to 50 boundary points before and after the Closest pt., shown in red in Fig. 10(b), are used to fit a line approximating and smoothing the grain boundary section corresponding to the Interrogated pt., which will be taken as the local boundary slope in the vicinity of the point of interest. The reason that we fit a line to a small subset of the boundary near each point, effectively locally smoothing the boundary, is that the noisy local variation of the EBSD-obtained boundaries would produce abrupt changes in local boundary normal that would lead to an extremely unrealistic noise being introduced in the rotated local strain fields. Finally, the angle α (grain-boundary angle) between the fitted line and the horizontal (x axis) is taken as the rotation angle and used in the coordinate transformation. Using this local angle α, which will change as we move along each boundary, we can rotate the DIC-measured strain field from the global (x, y) coordinate system to a local (n, t) coordinates, using:

$$\begin{bmatrix} \varepsilon_{tt} & \varepsilon_{tn} \\ \varepsilon_{tn} & \varepsilon_{nn} \end{bmatrix} = \begin{bmatrix} cos(\alpha) & sin(-\alpha) \\ sin(\alpha) & cos(\alpha) \end{bmatrix} \begin{bmatrix} \varepsilon_{xx} & \varepsilon_{xy} \\ \varepsilon_{xy} & \varepsilon_{yy} \end{bmatrix} \begin{bmatrix} cos(\alpha) & sin(-\alpha) \\ sin(\alpha) & cos(\alpha) \end{bmatrix}^{T}, \tag{2}$$

where the local ε_{nn} strain will now represent a normal strain across each boundary, the local ε_{tt} is the tangential strain along the boundary and the local ε_{tn} shear strain will represent two grains attempting to slide against each other, as illustrated schematically in Fig. 10(c). This procedure is repeated for every mantle point present in the DIC data, i.e., all the areas denoted by black in Fig. 10(d).

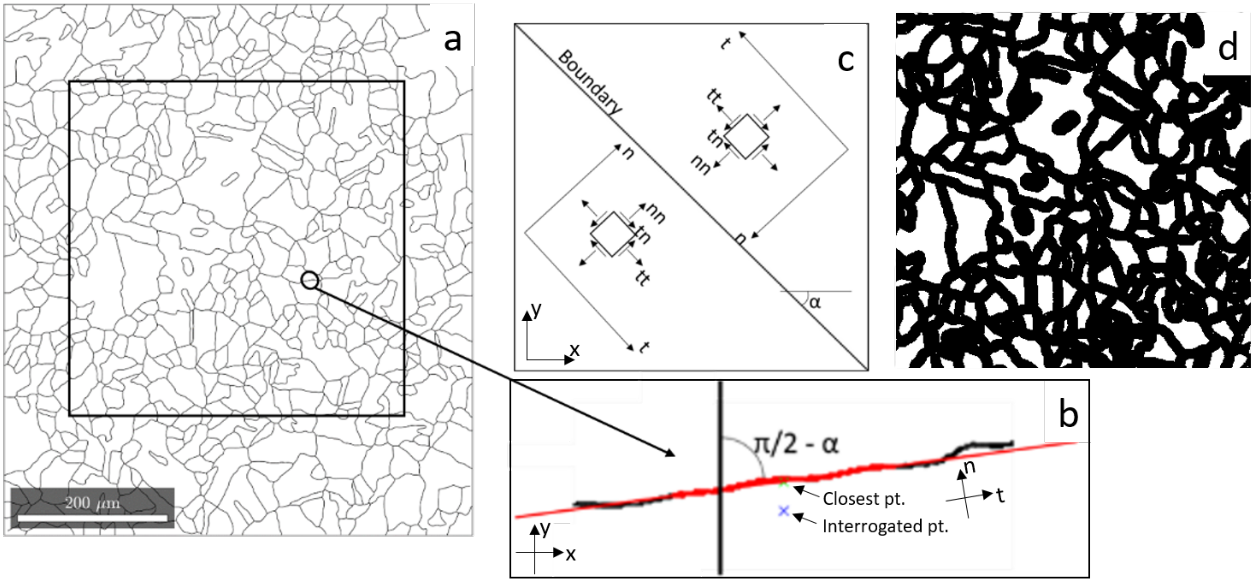

Fig. 10. (a) Grain boundaries obtained from EBSD; (b) How the angle α is obtained for a specific region of a specific GB; (c) Schematic of the coordinate systems (*x,y*) and (*n,t*); (d) The separation of mantle (in black) and core (in white).

Fig. 11 shows the strain fields before and after the coordinate transformation. Fig. 11(a) and (b) show the ε_{yy} and ε_{xy} components of residual strains for the entire region of interest; Fig. 11(c) shows contours only within the mantle regions of the same sample of the ε_{nn} (normal to the boundary) component of residual strain (the core is whited out); Fig. 11(d) shows the mantle-only contours of ε_{tn} (shearing the boundary) component of residual strain (again the core is whited out). In order to understand the advantage of using this coordinate system, Fig. 12 shows the magnified view of the boundary marked by the square in Fig. 11(a). From the local coordinate strains, shown in Fig. 12(c) and (d), it is clear that this specific boundary has relatively high residual shear strains and relatively low residual normal strains. This indicates that the two adjacent grains are being sheared against each other, instead of being pushed together or pulled apart. This observation is not as clear when observing the global coordinate strains shown in Fig. 12(a) and (b).

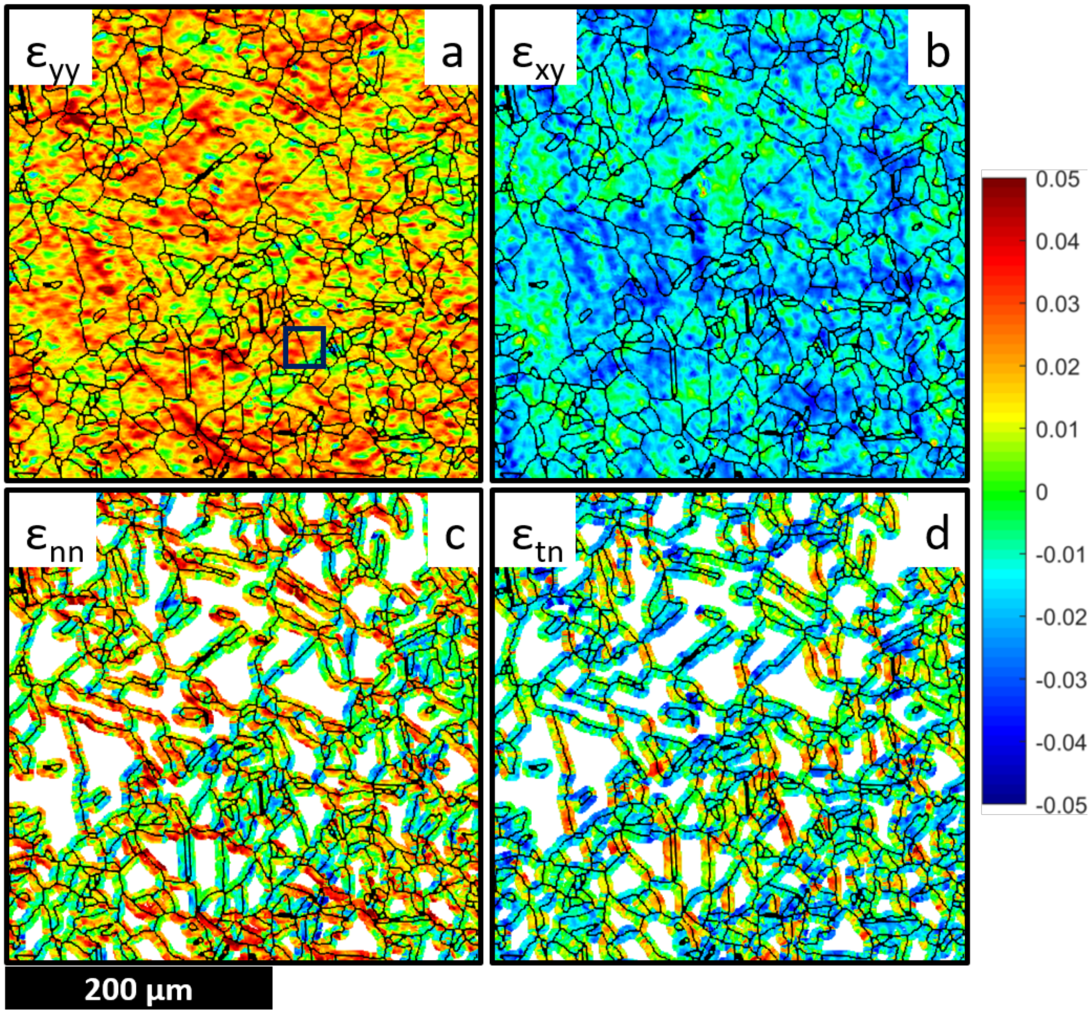

Fig. 11. (a) ε_{yy} component of residual strains; (b) ε_{xy} component of residual strains; (c) mantle-only ε_{nn} component of residual strains; (d) mantle-only ε_{tn} component of residual strains.

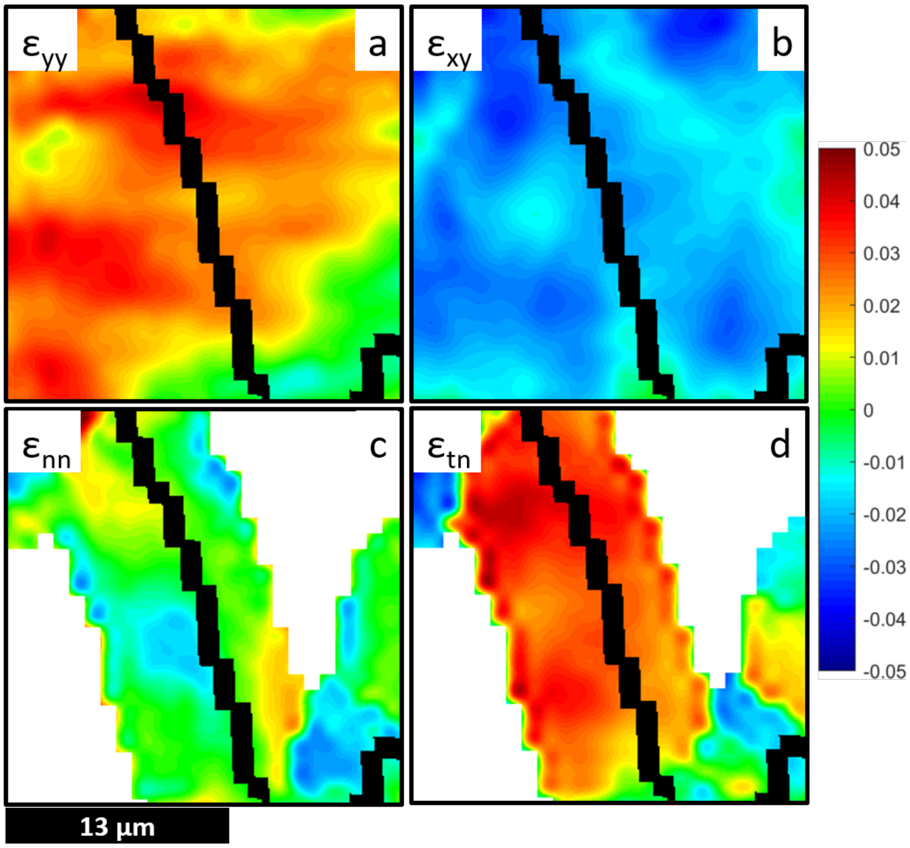

Fig. 12. Magnified view of the boundary marked with a square in Fig. 11(a).

A similar observation can be made about the local behavior at the mantle of each grain boundary. Collectively, and since we have a very large volume of local data form the high-resolution ex situ DIC measurements, by looking at all mantles of all grain boundaries contained within the region of interest, a conclusion can be drawn about the dominant deformation around grain boundaries under the different conditions. Fig. 13 shows normalized plots of the absolute value of the ratios between normal and shear residual strains ($|\varepsilon_{nn} : \varepsilon_{tn}| \,/\, max(|\varepsilon_{nn} : \varepsilon_{tn}|)$) at every investigated mantle point vs. the corresponding grain-boundary angle (α), for 3 different *elastic creep* loaded samples at three different temperatures (300°C, 500°C and 800°C). The roughly 50,000 plotted strain ratio points in each case are colored by the misorientation angle (defined as the difference between the crystallographic orientations of the two adjacent grains) of the corresponding boundary which can be obtained from the EBSD measurements. These results show that there is a relationship between the grain-boundary angle and the normal to shear strain ratio. Vertical and horizontal boundaries ($\alpha = 0, \pi/2, \pi\ldots$) possess higher ratios (i.e., relatively high local normal strains) while slanted boundaries present lower ratios (relatively high local shear strains). This localization effect at horizontal and vertical boundary angles becomes more pronounced as temperature increases, as seen by the sharper and narrower peaks in Fig. 13(c). Unlike what has been reported in some cases previously [31, 38], there is no clear observed correlation between misorientation angle and the local ratio of normal to shear strain: this material contains predominantly twin boundaries which have a misorientation angle of 60° and appear as dark red in Fig. 13. As seen from Fig. 13, these boundaries corresponding to red points show all levels of strain ratio. Finally, and perhaps most relevant to relating measured local mantle strains to underlying deformation mechanisms, as temperature increases there is a trend indicating that the strains at the mantles become more dominated by shear (i.e., lower overall ratios).

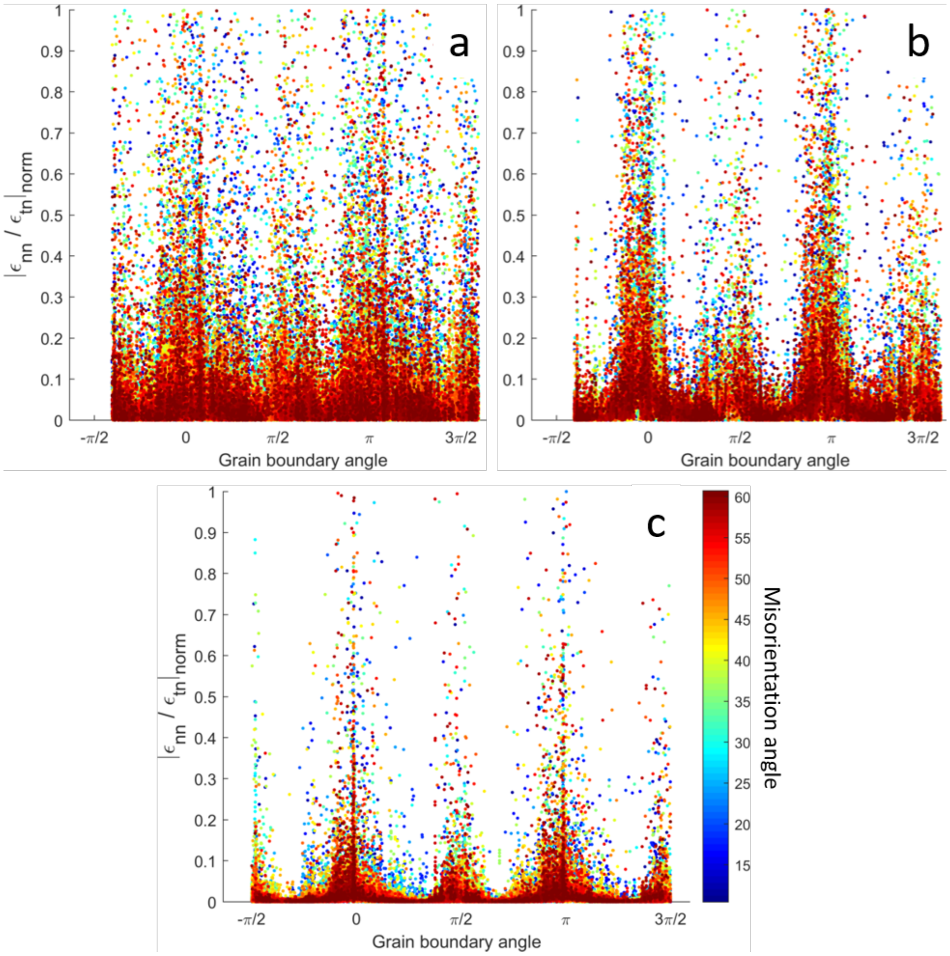

Fig. 13. (a) The ratio of normal to shear strains at mantle points vs the GB angle (α), colored by the misorientation angle on the closest boundary and normalized by the maximum ratio, for sample 3 (*elastic creep* at 300 °C); (b) sample 6 (*elastic creep* at 500 °C); (c) sample 9 (*elastic creep* at 800 °C).

To obtain a quantitative assessment, the average strain ratio at mantle regions for each case was calculated. Fig. 14 shows a bar plot of the average normal to shear strain ratios at the mantle regions for all samples. Here, we see that elastic creep loading presents a much lower average strain ratio than the plastic creep and plasticity cases, regardless of temperature levels. The results for plasticity and plastic creep were very similar, again indicating that plasticity dominates over creep at the load and temperature levels studied here (~25% above yield strengths for 23°C, 300°C and 500°C). Both these observations are consistent with the discussion from the RVE sizes accompanying Fig. 9. In fact, the two bar plots, Fig. 9 illustrating RVEs and Fig. 14 illustrating local strain ratio, are very similar in terms of the interrelations of the three different deformation types. In all cases, samples that had larger RVE sizes also presented higher ratios of normal to shear strains at the mantles. This observation also leads to the hypothesis that the size of the RVE (a measure of residual axial strain inhomogeneity) could be used as a proxy for detecting local mechanism transitions. At the macroscale, strong evidence that also points in this direction comes from the result for sample 9, which presents the lowest RVE size (lower degree of inhomogeneity) as well as the lowest average strain ratios (mantles dominated by shear). This result is corroborated by observations from Alomari et al. [39] who observed a change in creep mechanism for alloy 709 at around 650-700 °C (from dislocation climb dominated to grain boundary sliding dominated), by fitting power-law creep curves to experimental data at varying temperatures, and following Ashby [40] to predict the change of creep mechanism from a change in the stress exponent. In parallel, a fundamental interpretation of the behavior at the microscale can also provide an indication as to why prevalent grain boundary sliding might decrease the RVE size. With increased dominance of grain boundary sliding, the strains tend to accumulate mainly at the grain boundaries, and because the grain structure of the material is fairly uniform (with a large majority of boundaries being twin boundaries, a fairly uniform grain size distribution, and no preferential direction or texture to grain orientations), strains will form almost uniformly at grain boundaries making each grain, or a smaller collection of grains, exhibit a representative average response, thus resulting in a lower RVE size. In contrast, when grain boundary sliding is not the dominant mechanism and at least is less prevalent, the development of strains within the core regions of the grains becomes more significant, with slip bands that begin in one grain crossing multiple boundaries into other grains. With more deformation mechanisms now active, the formation of grain clusters might become more relevant, as was observed by Rotella and Sangid [41], for example. Formation of grain clusters would be one of the phenomena that makes the RVE size for plasticity larger than creep, although of course these microstructural conjectures cannot be proven from the results of this paper alone and would necessitate further study.

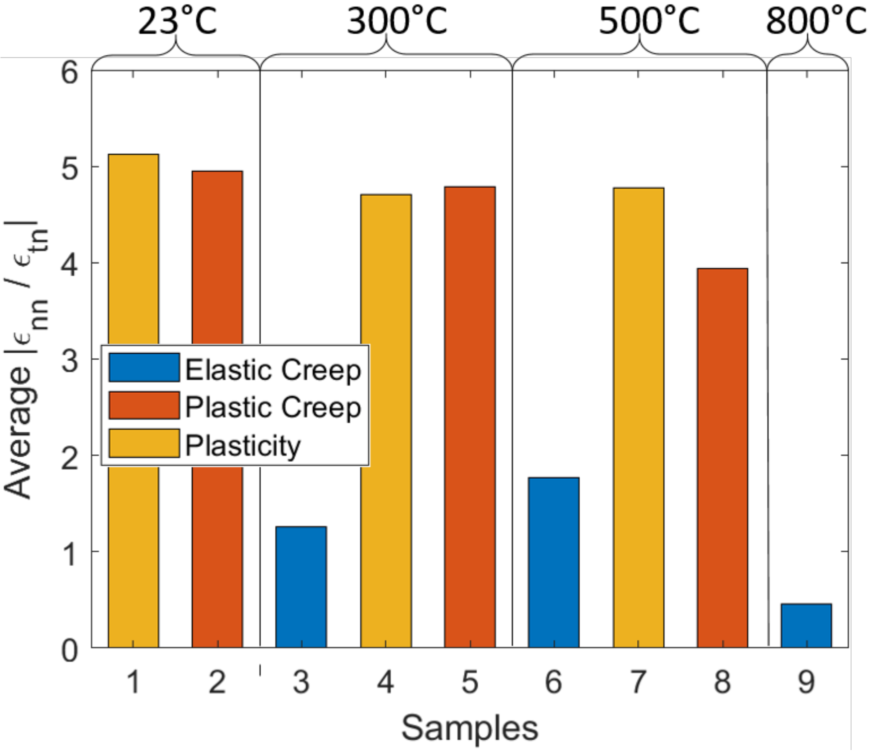

Fig. 14. Average strain ratios obtained for all samples.

5. Conclusions

The experimental study presented here, which involved high-resolution local strain measurement data combined with data analysis methods that borrowed concepts from numerical simulations, sought to investigate the influence of loading parameters on the degree of strain inhomogeneities present at the microscale. High-resolution DIC residual strain results and EBSD-obtained grain structure data were employed to measure the RVE sizes of samples loaded under a range of different loading parameters (maximum stress, temperature and hold time). These RVE measurements were made for three different deformation regimes namely *elastic creep, plastic creep* and *plasticity.* Further analysis of the strains at regions near grain boundaries (mantle points), using a relevant transformation of coordinates, allowed for the comparison between the measured RVE sizes and the nature of strain accumulation (measured by the local normal to shear strain ratio), which can be related to underlying deformation mechanisms, known to vary with loading conditions (especially temperature changes). A summary of the conclusions drawn from this study follows:

1) RVE sizes obtained for *elastic creep* were considerably lower than those obtained for *plasticity* and *plastic creep*;
2) Elastic creep RVE sizes were found to be within the range of 4-6 times the average grain size, in contrast with plastic RVE sizes in the range of 8-10;
3) Normal to shear strain ratios near grain boundaries (mantle regions) were calculated and showed a dependence on temperature, as expected since creep deformation mechanisms are known to be a function of temperature;
4) The average strain ratio for *elastic creep* was found to be much lower than that of *plasticity* and *plastic creep*, indicating that *elastic creep* presents more predominant grain boundary sliding, while *plasticity* seems to dominate the response whenever it is present;
5) The comparison between the RVE size and strain ratio results lead to the conclusion that the degree of inhomogeneity may be used as a proxy for determining deformation mechanism transitions. This is corroborated by the specific results for *elastic creep* at

higher temperature (800 °C), in agreement with literature findings on the creep mechanisms of the studied alloy.

Declaration of Competing Interest

The authors declare that they have no known competing financial interests or personal relationships that could have appeared to influence the work reported in this paper.

Acknowledgements

The work was carried out in part in the Materials Research Laboratory Central Research Facilities University of Illinois (EBSD measurements), and the Advanced Materials Testing and Evaluation Laboratory University of Illinois (mechanical testing). This research was performed in part using funding received from the Department of Energy Office of Nuclear Energy's Nuclear Energy University Program under grant number DE-NE0008436 (Project number 15-8432). This material is based upon work supported by the National Science Foundation under Grant No. CMMI 18-25466.

References

[1] C. Efstathiou, H. Sehitoglu and J. Lambros, "Multiscale strain measurements of plastically deforming polycrystalline titanium: Role of deformation heterogeneities," *International Journal of Plasticity,* vol. 26, no. 1, pp. 93-106, 2010.

[2] F. Delaire, J. L. Raphanel and C. Rey, "Plastic heterogeneities of a copper multicrystal deformed in uniaxial tension: Experimental study and finite element simulations," *Acta Materialia,* vol. 48, pp. 1075-1087, 2000.

[3] D. Raabe, M. Sachtleber, Z. Zhao, F. Roters and S. Zaefferer, "Micromechanical and macromechanical effects in grain scale polycrystal plasticity experimentation and simulation," *Acta Materialia,* vol. 49, pp. 3433-3441, 2001.

[4] F. Roters, P. Eisenlohr, L. Hantcherli, D. D. Tjahjanto, T. R. Bieler and D. Raabe, "Overview of constitutive laws, kinematics, homogenization and multiscale methods in crystal plasticity finite-element modeling: Theory, experiments, applications," *Acta Materialia,* vol. 58, pp. 1152-1211, 2010.

[5] R. Hill, "Elastic properties of reinforced solids: Some theoretical principles," *Journal of the Mechanics and Physics of Solids,* vol. 11, no. 5, pp. 357-372, 1963.

[6] A. Salahouelhadj and H. Haddadi, "Estimation of the size of the RVE for isotropic copper polycrystals by using elastic–plastic finite element homogenisation," *Computational Materials Science,* vol. 48, no. 3, pp. 447-455, 2010.

[7] M. Bouchedjra, T. Kanit, C. Boulemia, A. Amrouche and M. E. A. Belouchrani, "Determination of the RVE size for polycrystal metals to predict monotonic and cyclic elastoplastic behavior: Statistical and numerical approach with new criteria," *European Journal of Mechanics and Solids,* vol. 72, pp. 1-15, 2018.

[8] E. Nakamachi, N. N. Tam and H. Morimoto, "Multi-scale finite element analyses of sheet metals by using SEM-EBSD measured crystallographic RVE models," *International Journal of Plasticity,* vol. 23, pp. 450-489, 2007.

[9] S. I. Ranganathan and M. Ostoja-Starzewski, "Scale-dependent homogenization of inelastic random polycrystals," *Journal of Applied Mechanics,* vol. 75, no. 5, 051008-9, 2008.

[10] S. Ravindran, B. Koohbor and A. Kidane, "Experimental characterization of meso-scale deformation mechanisms and the RVE size in plastically deformed carbon steel," *Strain,* vol. 53, no. 1, e12217, 2017.

[11] J. C. Stinville, W. C. Lenthe, J. Miao and T. M. Pollock, "A combined grain scale elastic–plastic criterion for identification of fatigue crack initiation sites in a twin containing polycrystalline nickel-base superalloy," *Acta Materialia,* vol. 103, pp. 461-473, 2016.

[12] J. C. Stinville, W. C. Lenthe, M. P. Echlin, P. G. Callahan, D. Texier and T. M Pollock, "Microstructural statistics for fatigue crack initiation in polycrystalline nickel-base superalloys," *International Journal of Fracture,* vol. 208, pp. 221-240, 2017.

[13] A. Bagri, G. Weber, J. C. Stinville, W. C. Lenthe, T. M. Pollock, C. Woodward and S. Ghosh, "Microstructure and Property-Based Statistically Equivalent Representative Volume Elements for Polycrystalline Ni-Based Superalloys Containing Annealing Twins," *Metallurgical and Materials Transactions A,* vol. 49, no. 11, pp. 5727-5744, 2018.

[14] S. Yang, J. Dirrenberger, E. Monteiro and N. Ranc, "Representative volume element size determination for viscoplastic properties in polycrystalline materials," *International Journal of Solids and Structures,* vol. 158, pp. 210-219, 2019.

[15] A. Githens, S. Ganesan, Z. Chen, J. Allison, V. Sundararaghavan and S. Daly, "Characterizing microscale deformation mechanisms and macroscopic tensile properties of a high strength magnesium rare-earth alloy: A combined experimental and crystal plasticity approach," *Acta Materialia,* vol. 186, pp. 77-94, 2020.

[16] S. A. H. Motaman, F. Roters and C. Haase, "Anisotropic polycrystal plasticity due to microstructural heterogeneity: A multi-scale experimental and numerical study on additively manufactured metallic materials," *Acta Materialia,* vol. 185, pp. 340-369, 2020.

[17] J. Pelleg, "General Mechanisms of Creep," in *Creep in Ceramics. Solid Mechanics and Its Applications*, Springer, Cham, 2017.

[18] R. L. Bell and T. G. Langdon, "An investigation of grain-boundary sliding during creep," *Journal of mateiral science,* vol. 2, pp. 313-323, 1967.

[19] S. Upadhayay, H. Li, P. Bowen and A. Rabiei, "A study on tensile properties of Alloy 709 at various temperatures," *Material Science and Engineering A,* vol. 733, pp. 338-349, 2018.

[20] H. Naoi, H. Mimura, M. Ohgami, M. Sakakibara, S. Araki, Y. Sogoh, T. Ogawa, H. Sakurai and T. Fujita, "Development of tubes and pipes for ultra-supercritical thermal power plant boilers," *Nippon Steel Technical Report,* vol. 57, pp. 22-27, 1993.

[21] R. Ding, J. Yan, H. Li, S. Yu, A. Rabiei and P. Bowen, "Deformation microstructure and tensile properties of Alloy 709 at different temperatures," *Materials and Design,* vol. 176, 107843, 2019.

[22] T. Sourmail, H. K. D. H. Bhadeshia and D. J. C. MacKay, "Neural network model of creep strength of austenitic stainless steels," *Materials Science and Technology,* vol. 18, pp. 655-663, 2002.

[23] A. Lall, S. Sarkar, R. Ding, P. Bowen and A. Rabiei, "Performance of Alloy 709 under creep-fatigue at various dwell times," *Materials Science and Engineering: A,* vol. 761, 138028, 2019.

[24] N. Shaber, R. Stephens, J. Ramirez, G. P. Potirniche, M. Taylor, I. Charit and H. Pugesek, "Fatigue and creep-fatigue crack growth in alloy 709 at elevated temperatures," *Materials at High Temperatures,* vol. 36, no. 6, pp. 562-574, 2019.

[25] J. Carroll, W. Abuzaid, J. Lambros and H. Sehitoglu, "An experimental methodology to relate local strain to microstructural texture," *Review of Scientific Instruments,* vol. 81, no. 8, 083703-9, 2010.

[26] M. A. Sutton, W. J. Wolters, W. H. Peters, W. F. Ranson and S. R. McNeill, "Determination of displacements using an improved digital correlation method," *Image and vision computing,* vol. 1, no. 3, pp. 133-139, 1983.

[27] J. Schindelin, I. Arganda-Carreras, E. Frise, V. Kaynig, M. Longair, T. Pietzsc, S. Preibisch, C. Rueden, S. Saalfeld, B. Schmid, J-Y. Tinevez, D. J. White, V. Hartenstein, K. Eliceiri, P. Tomancak and A. Cardona, "Fiji: an open-source platform for biological image analysis," *Nature Methods,* vol. 9, no. 7, pp. 676-682, 2012.

[28] V. P. Rajan, M. N. Rossol and F. W. Zok, "Optimization of Digital Image Correlation for High-Resolution Strain Mapping of Ceramic Composites," *Experimental Mechanics*, vol. 52, pp. 1407-1421, 2012.

[29] B. Koohbor, S. Ravindran and A. Kidane, "Experimental determination of Representative Volume Element (RVE) size in woven composites," *Optics and Lasers in Engineering*, vol. 90, pp. 59-71, 2017.

[30] A. J. Wilkinson and T. B. Britton, "Strains, planes, and EBSD in materials science," *Materials Today,* vol. 15, no. 9, pp. 366-376, 2012.

[31] W. Abuzaid, M. Sangid, J. Carroll and H. Sehitoglu, "Slip transfer and plastic strain accumulation across grain boundaries in Hastelloy X," *Journal of the Mechanics and Physics of Solids,* vol. 60, no. 6, pp. 1201-1220, 2012.

[32] F. Di Gioacchino and J. Quinta da Fonseca, “An experimental study of the polycrystalline plasticity of austenitic stainless steel”, *International Journal of Plasticity*, vol. 74, p.p. 92-109, 2015.

[33] Y.B. Das, A. N. Forsey, T. H. Simm, K. M. Perkins, M. E. Fitzpatrick, S. Gungor and R. J. Moat, “In situ observation of strain and phase transformation in plastically deformed 301 austenitic stainless steel”, *Materials and Design*, vol. 112, p.p. 107-116, 2016.

[34] R. B. Vieira, “Strain Inhomogeneities During Plasticity and Creep of Metals: Representative Volume Elements and Microscale Strain Predictions”, Doctoral dissertation, University of Illinois at Urbana-Champaign, Urbana, 2021.

[35] S. Swaminathan, S. Ghosh and N. J. Pagano, "Statistically Equivalent Representative Volume Elements for Unidirectional Composite Microstructures: Part I - Without Damage," *Journal of Composite Materials,* vol. 40, no. 7, pp. 583-604, 2006.

[36] C. Liu, "On the Minimum Size of Representative Volume Element: An Experimental Investigation," *Experimental Mechanics,* vol. 45, no. 3, pp. 238-243, 2005.

[37] M. A. Meyersm and E. Ashworth, "A model for the effect of grain size on the yield stress of metals," *Philosophical Magazine A,* vol. 46, no. 5, pp. 737-759, 1982.

[38] K-S. Cheong and E. P. Busso, "Effects of lattice misorientations on strain heterogeneities in FCC polycrystals," *Journal of the Mechanics and Physics of Solids,* vol. 54, no. 4, pp. 671-689, 2006.

[39] A. S. Alomari, N. Kumar and K. L. Murty, "Investigation on Creep Mechanisms of Alloy 709," in *Proceedings of the ASME 2017 Nuclear Forum*, Charlotte, North Carolina, USA., 2017.

[40] M. Ashby, "A first report on deformation-mechanism maps," *Acta Metallurgica,* vol. 20, p.p. 887-897, 1972.

[41] J. Rotella and M. D. Sangid, “Microstructural-based strain accumulation during cyclic loading of Ni-based superalloys: The role of neighboring grains on interconnected slip bands,” *Fatigue & Fracture of Engineering Materials & Structures, vol.* 43, no. 10, pp. 2270-2286, 2020.